$Ni_{60}Nb_{40}$ Nanoglass for Tunable Magnetism and Methanol Oxidation

Ananya Baksi,* Sree Harsha Nandam, Di Wang, Robert Kruk, Mohammed Reda Chellali,
Julia Ivanisenko, Isabella Gallino, Horst Hahn, and Soumabha Bag*

ABSTRACT: Local control in microstructure in nanocrystalline solid
materials emerges from their property and reactivity. Similar observation is
also seen for nanostructured glassy alloys accounting for enhanced
properties of nanoglass compared to their metallic glass analogue. Here,
we show synthesis and detailed microstructural characterization of a
$Ni_{60}Nb_{40}$ nanoglass starting from amorphous nanoparticles and compared
the results with a melt spun ribbon (MSR) of identical atomic composition.
The effect on the magnetic property during the consolidation of glassy
nanoparticles at different uniaxial pressures to create such nanoglass is
studied in detail. While nanoglass showed ferromagnetic behavior at every
compaction pressure, the MSR always remained paramagnetic although its
density was comparable. Not only that the amorphous phase of these two
materials behaves differently, when annealed above their crystallization
temperature, annealed nanoglass responded distinctly differently compared
to the MSR confirming non identical local structure even after heat treatment. Taking advantage of the presence of amorphous
nickel, the enhanced response of the glassy interface in the nanoglass, we tested these materials for the electrochemical methanol
oxidation reaction (MOR) in alkaline medium and found that the nanoglass offers reasonably high MOR capacity compared to the
MSR. The structure–property correlation in the context of energy application using such nanoglass materials is tested for the first
time.

KEYWORDS: nanoglass, amorphous nickel, binary alloy, inert gas condensation, magnetism, electro oxidation
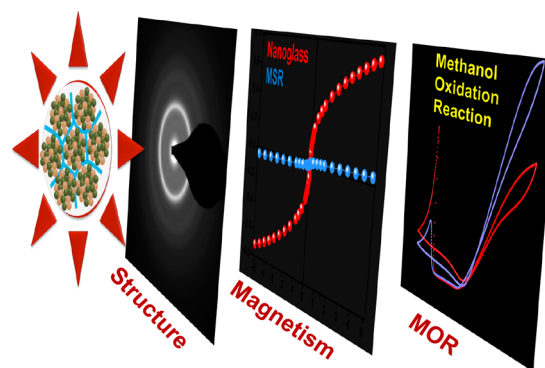
◼ INTRODUCTION

Alongside metallic glasses[1] in the melt spun ribbon (MSR) or
bulk form (BMG), "nanoglass",[2−4] a new class of nanoparticle
based glassy alloy system, is gaining interest due to its
distinctive and tunable properties.[5] The presence of glassy
interfaces among glassy grains in nanoglass as a result of
synthesis using an inert gas condensation (IGC)[6] method
followed by compaction led the path for modification and
identification of various properties in materials. Collectively,
these nanosized grains and the interfaces in nanoglasses
changed the structural,[7,8] biochemical,[9] mechanical,[4,10−12] and
magnetic properties[3,13] compared to conventional metallic
glasses (MSR) despite their identical chemical composition.
Mechanical property tailoring of Cu−Zr[4] nanoglasses includes
incorporation of glass−glass interfaces, modification of the
magnetic property of an Fe−Sc[5,14] alloy, or improving the
chemical response of Ni−Nb alloys toward electrochemical
glucose oxidation[15] as some exemplary outcomes in the
emerging field of metallic nanoglasses.

In most of the cases, enhanced properties are correlated to
the presence of glassy interfaces, and in some cases, they are
due to selective segregation of a particular element. Despite
these interesting observations and the efforts made by available
computational models,[16] several aspects of the structure and

property correlation of the materials remained unknown, for
example, the effect of diminishing influence of the glass−glass
interfaces in the property of nanoglass. The same effect can be
evaluated through a gradual increase in consolidation pressure
(reduction of free volume to tune properties) during synthesis
of a stable nanoglass. This type of study has not been carried
out so far on any nanoglasses.

To understand such an effect, $Ni_{60}Nb_{40}$, a stable well known
nickel based binary alloy, is an ideal candidate. This system has
already been studied in the form of an MSR, BMG, and thin
film due to its high stability and glass forming ability
(GFA).[17−19] $Ni_{60}Nb_{40}$ bulk metallic glass (BMG) is also
known for its high glass transition temperature (T_g = 895 K)
and Vicker's hardness (close to 7.8 GPa).[20] As a result, the
material was investigated in the past to determine its tensile
strength in its amorphous form. Additional effort to investigate

Scheme 1. Synthesis of Ni$_{60}$Nb$_{40}$ Nanoglass Following an Inert Gas Condensation Method
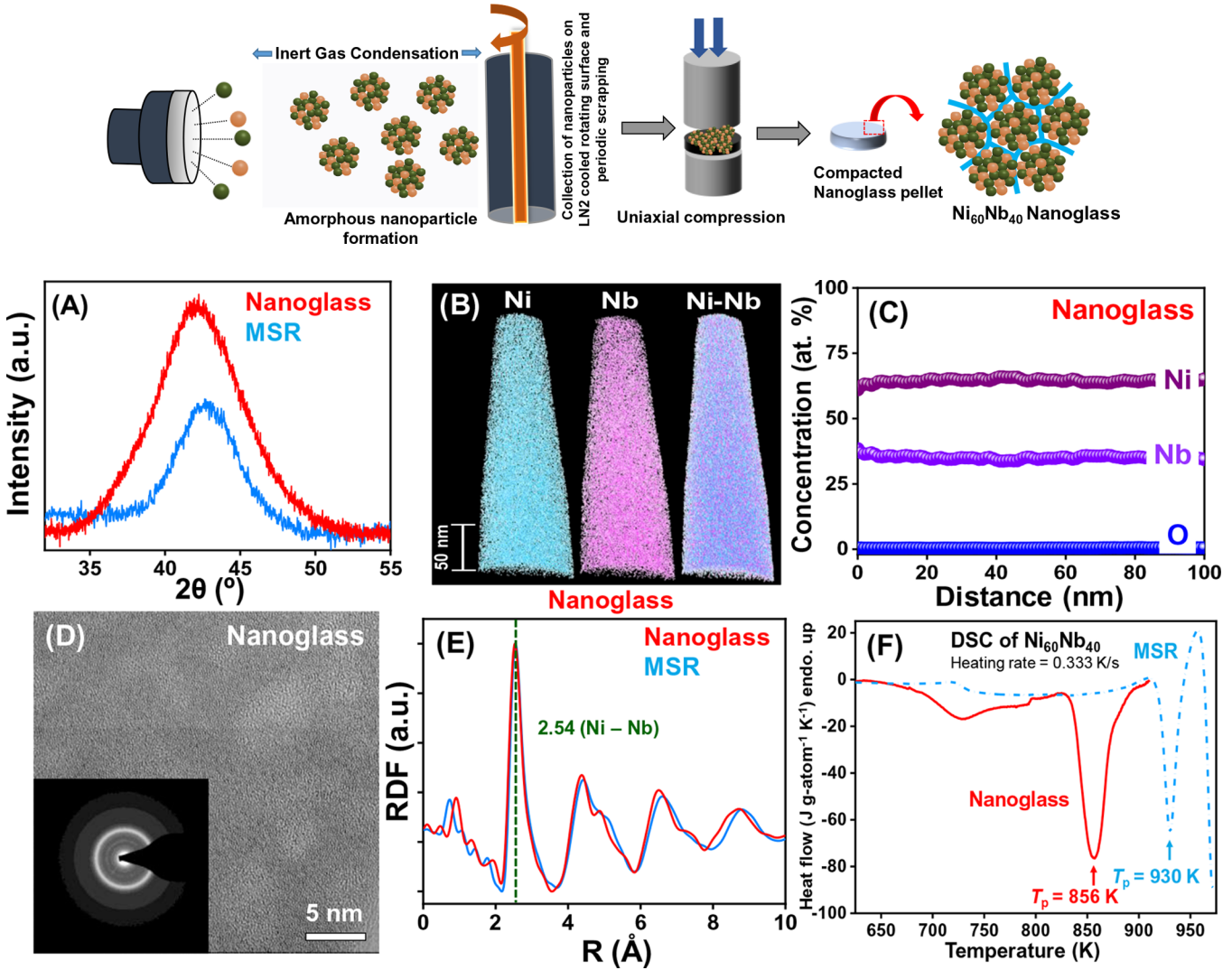
Figure 1. Characterization of Ni$_{60}$Nb$_{40}$ nanoglass. Featureless halo XRD signals in (A) confirm the amorphous nature of the melt spun ribbon (MSR) and nanoglass (compacted at 6 GPa) samples. APT measurement of the nanoglass sample in (B) and (C) confirms the uniform distribution of nickel and niobium throughout the sample. The microscopic (TEM) image (D) and SAED pattern (inset of (D)) further support the amorphous phase in it. (E) Radial distribution functions calculated from the SAED pattern of nanoglass and the MSR showing atomic packing (between Ni and Nb). (F) Thermographs obtained from differential scanning calorimetry showing different glass transition and crystallization temperatures of nanoglass and the MSR.

other interesting properties besides mechanical testing[20] has not been carried out extensively. Its weak magnetic response or paramagnetic behavior[21] and the difficulty to change the magnetic property of the MSR sample without changing the chemical composition[22] are the main reasons of lacking significant research interest in the field of magnetism.

Although such metallic glasses have been known for quite a long time, their chemical reactivity still has not been explored in detail. Besides tunable structure and properties (mechanical or magnetic), amorphous Ni based catalysts[23−26] are known to show better performance compared to their crystalline analogues. Due to the distinctive stability in aqueous medium,[27] few investigations are carried out to improve the chemical[28] and catalytic[29−31] activity of Ni$_{60}$Nb$_{40}$ metallic glasses upon introduction of additional elements. For example, Ni$_{60}$Nb$_{40}$ MSRs had been tested as anode materials to check their potential in fuel cell (FC)[29,32−35] applications. However, the material did not show exciting methanol oxidation reaction

(MOR)[36−39] activity. In order to enhance its efficiency, more elements, such as Pd, Pt, Ru, Co, Cu, Sn, etc.[29,40−43] were added to it, which led to a change in its chemical composition but marginally increased its MOR activity.

Here, we show a detailed study on the synthesis of metallic Ni$_{60}$Nb$_{40}$ nanoglass and determined its microstructure, thermal stability,[17,44] and magnetic property,[45] which are compared with an analogous MSR sample. Magnetic properties of the nanoglasses are carefully checked following the synthesis of different nanoglass pellets under varying consolidation pressures (1.6 to 8 GPa) to understand the diminishing effect of free volume on its magnetic property, which showed an inverse relation. The extended network of glassy interfaces throughout the sample is responsible for such enhanced magnetic behavior, which was also examined for electro chemical activity in alkaline medium. Electrochemical MOR activity of the nanoglass was found to be reasonably high compared to the MSR in identical experimental conditions.

RESULTS AND DISCUSSION

Microstructure Characterization. The $Ni_{60}Nb_{40}$ nano glass was synthesized using a magnetron sputtered IGC (or MS IGC) method reported elsewhere.[4] Briefly, the crystalline $Ni_{60}Nb_{40}$ target was sputtered in the presence of inert gases to create amorphous nanoparticles. Evaporated nanoparticles were collected on a liquid N_2 cooled rotating surface scrapped periodically. The collected nanoparticles were compacted by uniaxial pressure in a disk shaped pellet in situ form as shown in Scheme 1.

Several synthesis parameters were optimized using a $Ni_{60}Nb_{40}$ target, and five samples were made consisting approximately 100 mg of $Ni_{60}Nb_{40}$ nanopowder and four consolidated nanoglass pellets (1.6, 4, 6, and 8 GPa) at identical sputtering conditions following the abovementioned procedure. In situ compacted (at 1.6 GPa) pellets were further handled in ambient conditions, and additional compaction was made in ambient conditions (4, 6, and 8 GPa). All the nanoglass pellets were polished mechanically before the characterizations. All the measurements were done in triplicate. Structural characterization and thermal stability analysis of MSR and nanoglass compacted at 6 GPa are summarized in Figure 1. The amorphous nature of the materials, as shown in Figure 1A (other nanoglasses also showed similar broad features), is confirmed initially by X ray diffractograms (XRD) where both the nanoglass and the MSR show characteristic halo peaks.

The elemental distribution (Ni, Nb, and O) in the nanoglass was determined using APT mapping as shown in Figure 1B. Both Ni and Nb are uniformly distributed throughout the sample and no segregation was found when the elemental concentration analysis (Figure 1C) was done following the APT investigation for both the nanoglass and MSR (Figure S1). The nanoglass sample was almost oxygen free, and both Ni and Nb retained their target compositions as shown in the depth profile in Figure 1C. High resolution transmission electron microscopy (TEM) at several positions was performed to confirm the absence of any nanocrystallinity. Representative selected area electron diffraction (SAED) analysis is shown in the inset of Figure 1D. Local atomic arrangements were found by calculating the radial distribution function (RDF) derived from the SAED pattern (Figure 1E) of the nanoglass sample following recently developed techniques.[46] A similar study was done for the MSR sample as well, which matches with the RDF function of the nanoglass specimen (Figure 1E) and the previously studied glassy $Ni_{60}Nb_{40}$ alloys.[21,47] Besides the major peak at 2.54 Å (metallic bonding between nickel and niobium), secondary and tertiary order packed shells are found at 4.5 and 6.5 Å, respectively. However, small shoulders in the second and third peaks (Figure 1E) in the RDF of the nanoglass indicate a more medium range ordering compared to the MSR analogue. Hence, the first coordination shell for both the nanoglass and MSR are the same, while the second, third, and following shells differ slightly in terms of local ordering, which might be responsible for the different properties in nanoglass compared to the MSR (see later). No sharp peak below 2.54 Å was observed confirming the absence of any significant metal—oxygen bonding, which is in agreement with the APT analysis. The DSC curve of the nanoglass in Figure 1F shows an exothermic signal with an onset at 650 K, typical of glassy relaxation processes[48,49] that follows the main devitrification

exothermic signal with a glass transition temperature (T_g) at 820 K, onset of crystallization temperature (T_x) at 838 K, and crystallization peak temperature (T_p) at 856 K. In contrast to the nanoglass, the MSR shows characteristic temperature values that are at least 80° higher, i.e., T_g at 896 K, T_x at 920 K, and T_p at 933 K. The MSR shows in Figure 1F the onset of a second exothermic event with T_{p2} at 977 K (see DTA analysis, Figure S2), which is in accordance with previous analyses.[44]

Magnetic Property. After confirming the amorphous phase and its thermal stability against crystallization of the nanoglass material, the magnetic behavior of the as synthesized nanopowder and four nanoglass pellets (synthesized at different compaction pressures) was measured at various temperatures using a SQUID magnetometer and compared with MSR samples. The MSR sample was compressed separately to assess any change in magnetic properties. All the consolidated nanoglasses (coercivity of 130 and 107 Oe at 1.6 and 8 GPa, respectively) as well as the nanopowder (coercivity 174 Oe) showed weak ferromagnetism in terms of saturation magnetization values. Figure 2 The MSR exhibits
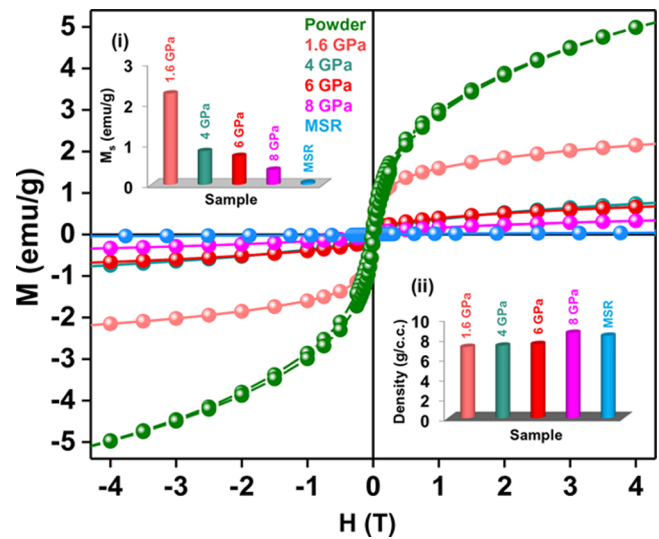
Figure 2. Magnetic behavior of the $Ni_{60}Nb_{40}$ amorphous alloys is studied. Ferromagnetic behavior is identified in the nanopowder and four nanoglass pellets at 5 K (compacted at 1.6, 4, 6, and 8 GPa). MSR showed paramagnetic behavior. In inset (i), saturation magnetization (M_S) of the materials is compared at 4 T. Densities of the samples at room temperature are shown in inset (ii).

paramagnetic behavior, which did not change even after successive compaction methods at 8 GPa. The saturation magnetization of the nanoglass showed an inverse relation with the increasing compaction pressure from 1.6 to 8 GPa as shown in Figure 2 inset i. An approximately 2.5 fold decrease in saturation magnetization was observed when the glassy nanopowders were compacted in situ at a 1.6 GPa pressure. The trend followed up to 4 GPa; beyond which, the effect of compaction pressure did not follow a linear relation with M_S values. The compaction pressure range for the current investigation was limited up to 8 GPa since the nanoglass pellet developed cracks during compaction beyond 8 GPa. Density of the materials increased with increasing compaction pressure as shown in Figure 2, inset ii, and reaches almost the expected physical density (8.56 g cc^{-1}) at 8 GPa (8.5 g cc^{-1}), which is close to that of the MSR (8.3 g cc^{-1}). At this

condition also, the M_S value was much higher for nanoglass than that of the MSR confirming the presence of glassy interfaces even at 8 GPa compaction pressure. We tried to extrapolate the M_S values with respect to the compaction pressure and found that at about 48 GPa, the nanoglass would have similar magnetism to that of the MSR. The density of the nanopowder sample was not measured due to its high reactivity in the ambient condition. Temperature dependent magnetic data of the sample prepared at 1.6 GPa is given in Figure S3.

Metallic nanoglasses are known to possess a network of glass−glass interfaces, which is absent in MSR materials. The difference in magnetic properties of nanoglasses and MSRs has been due to the microstructural origin.[3] In the present study, the glassy interfaces in nanoglass pellets and nanopowder materials significantly influence the overall magnetic (ferro magnetic) behavior of the materials, compared to the MSR sample. It is clear from Figure 2 that gradual reduction in the porosity/free volume (compared to the nanopowder material) of the nanoglass samples (pellets) takes place as the uniaxial pressure during compaction is enhanced (from 1.6 to 8 GPa), which is evident from the increased density (Figure 2, inset ii). At 8 GPa pressure, the materials found to be weakly ferromagnetic but possess comparable density with the paramagnetic MSR sample (inset ii of Figure 2) provide indirect proof of the presence of glassy nanograins with shared interfaces inside the nanoglass. Subsequent measurements in the current study were carried out with nanoglass pellets compressed at 6 GPa.

In order to understand the phase dependent change of magnetic behavior of the compressed materials against thermal energy (3 h heating at 1173 K or 900 °C, above the crystallization temperature recorded in Figure 1F), magnetic hysteresis loops of the as synthesized nanoglass (compressed at 6 GPa) and annealed samples are compared (Figure 3A,B).
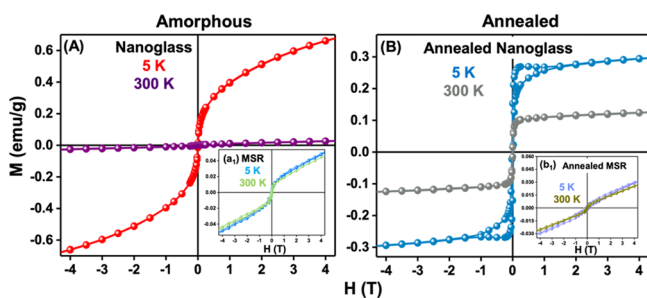
Figure 3. Temperature dependent magnetic behavior of the Ni$_{60}$Nb$_{40}$ (A) nanoglass and MSR (inset a$_1$) and annealed samples ((B) and inset b$_1$) is tested. Both amorphous and annealed nanoglass alloys showed enhanced magnetic ordering upon reduction of temperature from 300 to 5 K in (A) and (B). However, the paramagnetic behavior of MSR did not change significantly upon lowering the temperature (insets a$_1$ and b$_1$). Distinctive ferromagnetism was recorded in the annealed nanoglass sample, while a paramagnetic signal further weakened in the annealed MSR as shown in inset b$_1$.

From the SQUID measurement (Figure 3A) of the nanoglass, a nearly 6 fold increase in the overall magnetization is observed as the temperature is lowered from 300 to 5 K. Surprisingly, the MSR did not respond in the same way during SQUID measurement when temperature was reduced to 5 K from 300 K (inset a$_1$ of Figure 3A).

These samples were annealed separately above their respective crystallization temperatures as described before. XRD signals and Rietveld analysis (Figure S4) of the annealed nanoglass (Figure S4a) and MSR (Figure S4b) samples show the presence of an orthorhombic Ni$_3$Nb intermetallic phase (space group $PmmnS$) in majority. In the heated nanoglass sample, metal oxides (a mixture of NbO$_2$ and NiO) and a small amount of crystalline nickel (3.5 wt %) were identified. On the other hand, Rietveld analysis of the XRD of the heated MSR produced Ni$_6$Nb$_7$ (besides Ni$_3$Nb) in accordance with previous results.[50] Annealing of the MSR sample did not produce any metal oxide or pure metallic residue (nickel or niobium). The entire heating experiment was carried out in a vacuum tube (8×10^{-9} mbar), and oxidation of the samples (nanoglass and MSR) during heat treatment is unlikely. However, samples were exposed to aerial oxygen during their handling in ambient conditions. The oxides might have formed in the annealed nanoglass sample as a result of the reaction of the nanocrystalline multiphasic alloy (mixture of different nanostructured intermetallic components) with aerial oxygen. At high temperature, a reaction between the MSR and oxygen produces these metal oxides.[44]

When the magnetic behavior of the respective samples is checked, the overall saturation magnetization (M_S) of all the samples is reduced (Figure 3B) after annealing. In the annealed sample, Ni$_3$Nb is known to exhibit paramagnetic behavior.[51] At 5 K, the hysteresis loop of the annealed nanoglass (multiphase mixture of several components shown in Figure S4) showed a sudden jump of the signal near the magnetic coercive field (Figure 3B). This kind of behavior in hysteresis loops due to the contribution of tiny nanocrystalline Ni in the annealed sample appears when the sample is cooled below 50 K (Figure S5). The result also suggests the possibility of a presence of small amounts of nanocrystalline Ni in the nanoglass sample, which is further confirmed by Rietveld analysis (Figure S4). No change was recorded in the SQUID response of the annealed MSR sample (inset b$_1$ of Figure 3B) even upon reducing the temperature to 5 K from the room temperature.

Electrochemical Property and Application. The presence of amorphous Ni with possible protection due to Nb in alkaline medium prompted us to check the materials for electrochemical applications. Electrochemical oxidation ability of the as synthesized nanoglass sample is tested independently. In the presence of Ag/AgCl as a reference electrode (RE), cyclic voltammetry (CV) data of the materials are recorded (Figure 4) where they are used as a working electrode (WE) and platinum (Pt) as a counter electrode in the presence of 4 M methanol (CH$_3$OH) in alkaline medium. The scan rate dependent performance of the nanoglass (consolidated at 6 GPa) electrode in alkaline medium had been carried out already and reported recently in the context of nonenzymatic glucose sensing using the nanoglass.[15] During the current study, the scan rate is maintained at 50 mV s^{-1}. Sweeping from −0.2 V to +0.8 V, the nanoglass showed 9.3 mA cm^{-2} current density (at −0.07 V vs Ag/AgCl) in the presence of 4 M methanol in 0.1 M NaOH solution. Repetition of the same experiment with the MSR sample results the current density to be 3 mA cm^{-2} (Figure 4). The electrochemical behavior of the nanoglass and MSR in the absence of methanol is shown in inset i of Figure 4.

The anodic and cathodic peaks in Figure 4i appear due to the interconversion of the NiO(OH)/Ni(OH)$_2$ system in the alkaline medium. However, upon addition of methanol, its CV
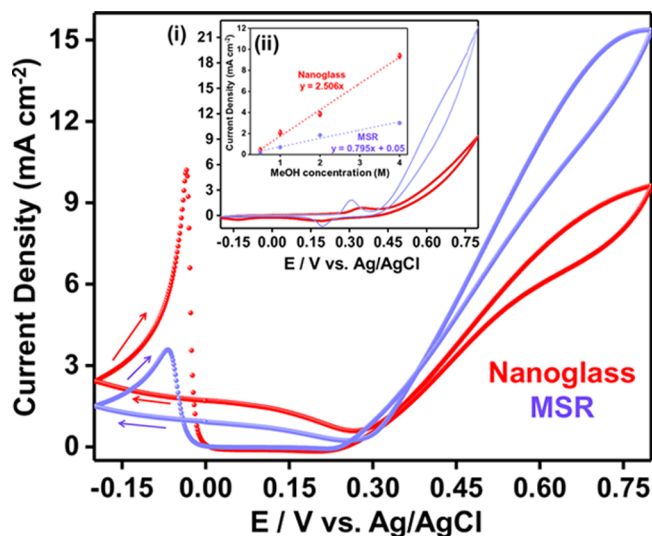
Figure 4. The electrochemical methanol oxidation (MOR) ability of the nanoglass in alkaline medium is studied and compared with MSR. Cyclic voltammetry (CV) with the nanoglass as a working electrode (WE) shows a distinctive response in 4 M methanol in 0.1 M NaOH solution compared to the MSR sample. Inset (i) represents the performance of the nanoglass and MSR in the alkaline medium in the absence of methanol (scan rate of 50 mV s^{-1}). Results of the concentration dependent (0.5, 1, 2, and 4 M methanol) electro chemical oxidation study using the two electrodes are summarized in inset (ii).

curves change significantly. Separate measurements with four different methanol solutions (0.5, 1, 2, and 4 M) show a clear indication (Figure S6) of their ability for the electrochemical oxidation process. The oxidative current density was propor tional to the methanol concentration (0.5 to 4 M methanol in 0.1 N NaOH solution). The methanol oxidation mechanism in the presence of nickel is known and explained elsewhere.[52−54] The well defined anodic peak appeared close to 0 V following the oxidation of freshly chemisorbed species (contributed from methanol) on the electrode. Results in Figure 4ii show that both of these materials can be used for the oxidation process; however, the nanoglass response is better for the reaction in alkaline medium. Nanoglass (compressed at 6 GPa) offers 2.5 mA cm^{-2} M^{-1} sensitivity for the oxidation process in contrast to the MSR electrode, which shows only 0.79 mA cm^{-2} M^{-1} sensitivity for the same reaction. Overall, higher current density and good linear behavior [R^2 (adj.) = 0.993 for nanoglass and R^2 (adj.) = 0.956 for MSR specimen] are recorded in the methanol concentration dependent MOR study for the nanoglass sample. Table 1 shows the distinctive MOR response of the nanoglass electrode in alkaline conditions. Among other materials, only HF treated doped metallic glass (Ni$_{59}$Nb$_{40}$Pt$_{0.6}$Sn$_{0.4}$) shows[42] better methanol electro oxidation activity. The measurement also points toward the underlying

potential of the nickel based amorphous family of binary alloys as anode materials for the methanol oxidation reaction (MOR) and similar other energy related application.[55]

SUMMARY AND CONCLUSIONS

In summary, a detailed investigation on the microstructure and various application oriented properties (magnetic and electro chemical methanol oxidation activity) of the Ni$_{60}$Nb$_{40}$ nanoglass is shown and compared with a melt spun ribbon (MSR) sample in the current study for the first time. Combined XRD, TEM, and APT analysis shows a uniform atomic distribution of nickel and niobium and an amorphous phase in the samples. Radial distribution function (RDF) analysis shows the presence of Ni−Nb metallic bonding in the sample. Results of the DSC analysis of the nanoglass sample at a 20 K min^{-1} heating rate show distinctive early devitrification with an onset of crystallization at 838 K, which is 82 K lower than the analogous characteristic temperature of the MSR glassy material. Mechanical (compaction) and thermal energy dependent change in saturation magnetization (M_S) in this nanoglass sample is also demonstrated for the first time. Annealing of the nanoglass further reduces the M_S value, but the sample shows a weak trace of ferromagnetism probably due to the presence of small amounts of metallic Ni. The methanol oxidation reaction (MOR) is studied electrochemically using the nanoglass and MSR as working electrodes separately, and their performance is compared with that of the MSR sample in alkaline conditions. Nanoglass shows greater oxidation ability than that of the MSR sample; however, both the samples have potential as anodes in the electrochemical MOR.

MATERIALS AND METHODS

Chemicals. A Ni$_{60}$Nb$_{40}$ target (99.9% purity from MaTeck GmbH) was used during the magnetron sputtering experiments. Approximately 99% purity methanol from VWR GmbH was used for the methanol oxidation reactions (MOR). Sodium hydroxide (NaOH) with 99.9% purity was received from Sigma Aldrich GmbH. Deoxygenated MilliQ water (18.2 MΩ) was used to prepare the solutions during the study. All the chemicals were used as received without further purification.

Synthesis. The nanoglass preparation method is illustrated in Scheme 1. The Ni$_{60}$Nb$_{40}$ target was sputtered in the presence of inert gases (He and Ar) at 0.3 mbar of pressure. The glassy nanoparticles were condensed by the inert gas followed by collection on a liquid nitrogen cooled surface and consolidation at 1.6 GPa in vacuum to produce a thin pellet of approximately 0.25 mm in thickness. Three other pellets (compacted at 4, 6, and 8 GPa) were made following additional uniaxial compaction in ambient conditions. A nanopowder sample with an identical composition was also synthesized and handled in inert conditions for further analysis. The melt spun ribbon (MSR) sample was prepared upon cooling the molten nickel and niobium mixed with a 60:40 atomic ratio on a rotating copper wheel.

Characterization. All samples were characterized using standard techniques. A Bruker X ray diffractometer equipped with a Cu Kα X ray source was used for X ray diffraction (XRD) studies. Heating

Table 1. Electrochemical Methanol Oxidation Activity Using the Ni−Nb Based Electrode

materials	phase	reference electrode	medium	highest current density (mA cm^{-2})	reference
Ni$_{59}$Nb$_{40}$Pt$_{0.6}$Ru$_{0.4}$	amorphous	Ag/AgCl	1 M HClO$_4$	0.2	41
Ni$_{59}$Nb$_{40}$Pt$_{0.6}$Sn$_{0.4}$ (90 s HF treated)	amorphous	Ag/AgCl	1 M H$_2$SO$_4$	12.25	42
Ni$_{59}$Nb$_{40}$Pt$_{0.6}$Sn$_{0.4}$	amorphous	Ag/AgCl	1 M H$_2$SO$_4$	0.26	42
Ni$_{60}$Nb$_{40}$ (melt-spun ribbon)	amorphous	Ag/AgCl	0.1 M NaOH	3	this work
Ni$_{60}$Nb$_{40}$ (nanoglass)	amorphous	Ag/AgCl	0.1 M NaOH	9.3	this work

experiments of the samples were done separately inside a quartz tube maintained at 8×10^{-9} mbar. The vacuum tube was constantly pumped using a turbo molecular pump throughout the heating experiment. The Rietveld analysis is carried out on the XRD patterns of annealed samples using TOPAS 5 to determine the lattice parameters, phase compositions, crystallite sizes, etc. An image aberration corrected FEI Titan 80−300 transmission electron micro scope (TEM) operated at 300 kV was used for structural characterization at nanometer and atomic scales. Thin TEM specimens were prepared using a focused ion beam (FIB) on an FEI Strata dual beam system. The needle shaped samples for atom probe tomography (APT) were prepared by an annular milling method with a typical radius of curvature of approximately 100 nm and a standard lift out method[56] using a Zeiss Auriga 60FIB. Needle shaped APT samples were prepared with an annular milling method with a typical radius of curvature of approximately 100 nm. The APT measurements were carried out using a Cameca LEAP 4000X HR instrument in the laser pulsing mode (λ = 355 nm, pulse frequency of 100 kHz, sample temperature of 50 K, pulse energy of 50 pJ, and evaporation rate at 0.5%). The reconstruction of the APT data was performed with IVAS 3.6.14. The calorimetric measurements were carried out in a power compensated PerkinElmer differential scanning calorimeter (Diamond DSC) and in a Netzsch STA 449C Jupiter differential thermal analyzer (DTA).[44] The scans were carried out with a heating rate of 0.333 K s^{-1} under a constant argon gas flow using copper crucibles (for DSC scans) and graphite crucibles (for DTA scans). The magnetic measurements were carried out using a superconducting quantum interference device (SQUID) magneto meter of the Quantum Design Company (model: MPMS XL).[3] The capsules for magnetic measurement were prepared inside a glovebox and transported to the instrument in an argon filled container. Bulk densities of these as prepared samples (MSR and nanoglasses) were measured using a well known liquid displacement method (in dimethyl phthalate as the liquid medium) based on the Archimedes principle. The density of the dimethyl phthalate (1.19 g cc^{-1}) was used to calculate the density of the MSR and pellets.

Electrochemical Cell Configuration. A general purpose electro chemical system (from μAutolab type III) coupled to a three electrode electrochemical cell was used to carry out all the electrochemical methanol oxidation tests. $Ni_{60}Nb_{40}$ amorphous alloys (MSR and nanoglass) were used as working electrodes (WEs), platinum foil as the counter electrode (CE), and Ag/AgCl as the reference electrode (RE). A gold wire of 0.10 mm in diameter connected the working electrodes (pellets of nanoglass or MSR).

Cyclic Voltammetry. Cyclic voltammetric (CV) studies were performed with different concentrations of methanol (0.5 M to 4 M) prepared in 0.1 M NaOH at room temperature (25 °C) in a 50 mL cell. The scan voltage range was fixed between −0.2 and +0.8 V for the current study. Current density values reported in this work were evaluated based on geometric surface areas of the amorphous alloys. All the electrode potentials that appeared in this report were calculated with respect to the Ag/AgCl electrode.

■ **AUTHOR INFORMATION**

Corresponding Authors

Ananya Baksi − *Institute of Nanotechnology, Karlsruhe Institute of Technology, Eggenstein Leopoldshafen 76344, Germany;* ⊙ orcid.org/0000 0003 3328 4399; Email: ananya.baksi@kit.edu

Soumabha Bag − *Institute of Nanotechnology, Karlsruhe Institute of Technology, Eggenstein Leopoldshafen 76344, Germany;* ⊙ orcid.org/0000 0002 0932 105X; Email: soumabha.bag@kit.edu

Authors

Sree Harsha Nandam − *Institute of Nanotechnology, Karlsruhe Institute of Technology, Eggenstein Leopoldshafen 76344, Germany*

Di Wang − *Institute of Nanotechnology and Karlsruhe Nano Micro Facility, Karlsruhe Institute of Technology, Eggenstein Leopoldshafen 76344, Germany;* ⊙ orcid.org/0000 0001 9817 7047

Robert Kruk − *Institute of Nanotechnology, Karlsruhe Institute of Technology, Eggenstein Leopoldshafen 76344, Germany*

Mohammed Reda Chellali − *Institute of Nanotechnology, Karlsruhe Institute of Technology, Eggenstein Leopoldshafen 76344, Germany*

Julia Ivanisenko − *Institute of Nanotechnology, Karlsruhe Institute of Technology, Eggenstein Leopoldshafen 76344, Germany*

Isabella Gallino − *Chair of Metallic Materials, Saarland University, Saarbrücken 66123, Germany*

Horst Hahn − *Institute of Nanotechnology, Karlsruhe Institute of Technology, Eggenstein Leopoldshafen 76344, Germany; Herbert Gleiter Institute of Nanoscience, Nanjing University of Science and Technology, Nanjing 210094, P. R. China;* ⊙ orcid.org/0000 0001 9901 3861

Author Contributions

A.B. and S.B. have designed and performed the experiments and interpreted the results. S.H.N. had helped in magnetron sputtering experiments during nanoglass synthesis. D.W. performed the TEM characterization and helped in micro structure analysis. R.K. helped in analyzing the SQUID data. M.R.C. performed the APT measurements. I.G. had carried out the calorimetric study on the samples and helped interpret the data. A.B. and S.B. wrote the manuscript with input from all the co authors. The entire project was carried out under H.H.'s supervision.

Notes

The authors declare no competing financial interest.

■ **REFERENCES**

(1) Wang, W. H.; Dong, C.; Shek, C. H. Bulk metallic glasses. *Mater. Sci. Eng., R* **2004**, *44*, 45−89.

(2) Gleiter, H. Nanoglasses: a new kind of noncrystalline materials. *Beilstein J. Nanotechnol.* **2013**, *4*, 517−533.

(3) Witte, R.; Feng, T.; Fang, J. X.; Fischer, A.; Ghafari, M.; Kruk, R.; Brand, R. A.; Wang, D.; Hahn, H.; Gleiter, H. Evidence for enhanced ferromagnetism in an iron based nanoglass. *Appl. Phys. Lett.* **2013**, *103*, 073106−073106.

(4) Nandam, S. H.; Ivanisenko, Y.; Schwaiger, R.; Śniadecki, Z.; Mu, X.; Wang, D.; Chellali, R.; Boll, T.; Kilmametov, A.; Bergfeldt, T.; Gleiter, H.; Hahn, H. Cu Zr nanoglasses: Atomic structure, thermal stability and indentation properties. *Acta Mater.* **2017**, *136*, 181−189.

(5) Fang, J. X.; Vainio, U.; Puff, W.; Wurschum, R.; Wang, X. L.; Wang, D.; Ghafari, M.; Jiang, F.; Sun, J.; Hahn, H.; Gleiter, H. Atomic structure and structural stability of Sc75Fe25 nanoglasses. *Nano Lett.* **2012**, *12*, 458−463.

(6) Jing, J.; Krämer, A.; Birringer, R.; Gleiter, H.; Gonser, U. Modified atomic structure in a palladium iron silicon nanoglass. A Moessbauer study. *J. Non Cryst. Solids* **1989**, *113*, 167−170.

(7) Wang, X. L.; Jiang, F.; Hahn, H.; Li, J.; Gleiter, H.; Sun, J.; Fang, J. X. Plasticity of a scandium based nanoglass. *Scr. Mater.* **2015**, *98*, 40−43.

(8) Wang, X.; Jiang, F.; Hahn, H.; Li, J.; Gleiter, H.; Sun, J.; Fang, J. Sample size effects on strength and deformation mechanism of Sc75Fe25 nanoglass and metallic glass. *Scr. Mater.* **2016**, *116*, 95−99.

(9) Chen, N.; Shi, X.; Witte, R.; Nakayama, K. S.; Ohmura, K.; Wu, H.; Takeuchi, A.; Hahn, H.; Esashi, M.; Gleiter, H.; Inoue, A.; Louzguine, D. V. A novel Ti based nanoglass composite with submicron nanometer sized hierarchical structures to modulate osteoblast behaviors. *J. Mater. Chem. B* **2013**, *1*, 2568−2574.

(10) Wang, C.; Cao, Q. P.; Wang, X. D.; Zhang, D. X.; Qu, S. X.; Jiang, J. Z. Stress dependent shear transformation zone in Ni Nb thin film metallic glass and its correlation with deformation mode transition. *Scr. Mater.* **2016**, *122*, 59−63.

(11) Hu, Q.; Wu, J.; Zhang, B. Synthesis and nanoindentation behaviors of binary CuTi nanoglass films. *Phys. B* **2017**, *521*, 28−31.

(12) Nandam, S. H.; Adjaoud, O.; Schwaiger, R.; Ivanisenko, Y.; Chellali, M. R.; Wang, D.; Albe, K.; Hahn, H. Influence of topological structure and chemical segregation on the thermal and mechanical properties of Pd Si nanoglasses. *Acta Mater.* **2020**, *193*, 252−260.

(13) Ghafari, M.; Hahn, H.; Gleiter, H.; Sakurai, Y.; Itou, M.; Kamali, S. Evidence of itinerant magnetism in a metallic nanoglass. *Appl. Phys. Lett.* **2012**, *101*, 243104−243104.

(14) Wang, C.; Wang, D.; Mu, X.; Goel, S.; Feng, T.; Ivanisenko, Y.; Hahn, H.; Gleiter, H. Surface segregation of primary glassy nanoparticles of Fe90Sc10 nanoglass. *Mater. Lett.* **2016**, *181*, 248−252.

(15) Bag, S.; Baksi, A.; Nandam, S. H.; Wang, D.; Ye, X.; Ghosh, J.; Pradeep, T.; Hahn, H. Nonenzymatic Glucose Sensing Using Ni60Nb40 Nanoglass. *ACS Nano* **2020**, *14*, 5543−5552.

(16) Adjaoud, O.; Albe, K. Microstructure formation of metallic nanoglasses: Insights from molecular dynamics simulations. *Acta Mater.* **2018**, *145*, 322−330.

(17) Xia, L.; Li, W. H.; Fang, S. S.; Wei, B. C.; Dong, Y. D. Binary Ni Nb bulk metallic glasses. *J. Appl. Phys.* **2006**, *99*, 026103−026103.

(18) Ruhl, R. C.; Giessen, B. C.; Cohen, M.; Grant, N. J. Metastable hexagonal close packed phases in nickel rich nickel niobium and nickel tantalum alloys. *J. Less Common Metals* **1967**, *13*, 611−618.

(19) Ruhl, R. C.; Giessen, B. C.; Cohen, M.; Grant, N. J. New microcrystalline phases in the niobium nickel and tantalum nickel systems. *Acta Met.* **1967**, *15*, 1693−1702.

(20) Zhu, Z.; Zhang, H.; Pan, D.; Sun, W.; Hu, Z. Fabrication of binary Ni Nb bulk metallic glass with high strength and compressive plasticity. *Adv. Eng. Mater.* **2006**, *8*, 953−957.

(21) Bag, S.; Baksi, A.; Wang, D.; Kruk, R.; Benel, C.; Chellali, M. R.; Hahn, H. Combination of pulsed laser ablation and inert gas condensation for the synthesis of nanostructured nanocrystalline, amorphous and composite materials. *Nanoscale Adv.* **2019**, *1*, 4513−4521.

(22) Danilov, D.; Hahn, H.; Gleiter, H.; Wenzel, W. Mechanisms of Nanoglass Ultrastability. *ACS Nano* **2016**, *10*, 3241−3247.

(23) Salinas Torres, D.; Nozaki, A.; Navlani García, M.; Kuwahara, Y.; Mori, K.; Yamashita, H. Recent Applications of Amorphous Alloys to Design Skeletal Catalysts. *Bull. Chem. Soc. Jpn* **2020**, *93*, 438−454.

(24) Wang, Z. J.; Li, M. X.; Yu, J. H.; Ge, X. B.; Liu, Y. H.; Wang, W. H. Low Iridium Content IrNiTa Metallic Glass Films as Intrinsi

cally Active Catalysts for Hydrogen Evolution Reaction. *Adv. Mater.* **2019**, *32*, 1906384.

(25) Jiang, R.; Tran, D. T.; McClure, J. P.; Chu, D. A class of (Pd Ni P) electrocatalysts for the ethanol oxidation reaction in alkaline media. *ACS Catal.* **2014**, *4*, 2577−2586.

(26) Huang, J. J.; Hwang, W. S.; Weng, Y. C.; Chou, T. C. Electrochemistry of ethanol oxidation on Ni Pt alloy electrodes in KOH solutions. *Mater. Trans.* **2009**, *50*, 1139−1147.

(27) Grant, N. C.; Archer, M. D. The electrochemistry of glassy 60Ni 40Nb in aqueous media. *J. Electrochem. Soc.* **1984**, *131*, 997−1003.

(28) Jayalakshmi, S.; Vasantha, V. S.; Fleury, E.; Gupta, M. Characteristics of Ni Nb based metallic amorphous alloys for hydrogen related energy applications. *Appl. Energy* **2012**, *90*, 94−99.

(29) Sánchez, M.; Pierna, A. R.; Ruiz, N.; Barroso, J.; Del Val, J. J. Amorphous catalysts based on (NiNb)99(Pt X Y)1 for DAFC using ethanol and bioethanol as fuels. *Int. J. Hydrogen Energy* **2014**, *39*, 3991−3996.

(30) Barranco, J.; Pierna, A. R. On the enhancement of methanol and CO electro oxidation by amorphous (NiNb)PtSnRu alloys versus bifunctional PtRu and PtSn alloys. *J. Non Cryst. Solids* **2008**, *354*, 5153−5155.

(31) Kawashima, A.; Kanda, T.; Hashimoto, K. Amorphous alloy catalysts for electrooxidation of methanol and its derivatives in a sulfuric acid solution. *Mater. Sci. Eng.* **1988**, *99*, 521−524.

(32) Sánchez, M.; Pierna, A. R.; Lorenzo, A.; Del Val, J. J. Effect of cocatalyst and composition on catalytic performance of amorphous alloys for ethanol electrooxidation and PEMFCs. *Int. J. Hydrogen Energy* **2016**, *41*, 19749−19755.

(33) Koenigsmann, C.; Wong, S. S. One dimensional noble metal electrocatalysts: a promising structural paradigm for direct methanol fuel cells. *Energy Environ. Sci.* **2011**, *4*, 1161−1176.

(34) Zhao, F.; Yuan, Q.; Luo, B.; Li, C.; Yang, F.; Yang, X.; Zhou, Z. Surface composition tunable octahedral PtCu nanoalloys advance the electrocatalytic performance on methanol and ethanol oxidation. *Sci. China Mater.* **2019**, *62*, 1877−1887.

(35) Vasantha, V. S.; Chin, H. S.; Fleury, E. Corrosion properties of Ni Nb & Ni Nb M (M = Zr, Mo, Ta & Pd) metallic glasses in simulated PEMFC conditions. *J. Phys.: Conf. Ser.* **2009**, *144*, No. 012008.

(36) Zhao, Y.; Liu, J.; Liu, C.; Wang, F.; Song, Y. Amorphous CuPt Alloy Nanotubes Induced by Na2S2O3as Efficient Catalysts for the Methanol Oxidation Reaction Amorphous CuPt Alloy Nanotubes Induced by Na2S2O3 as Efficient Catalysts for the Methanol Oxidation Reaction. *ACS Catal.* **2016**, *6*, 4127−4134.

(37) Jiang, K.; Bu, L.; Wang, P.; Guo, S.; Huang, X. Trimetallic PtSnRh Wavy Nanowires as Efficient Nanoelectrocatalysts for Alcohol Electrooxidation. *ACS Appl. Mater. Interfaces* **2015**, *7*, 15061−15067.

(38) Ren, G.; Liu, Y.; Wang, W.; Wang, M.; Zhang, Z.; Liang, Y.; Wu, S.; Shen, J. Facile Synthesis of Highly Active Three Dimensional Urchin like Pd@PtNi Nanostructures for Improved Methanol and Ethanol Electrochemical Oxidation. *ACS Appl. Nano Mater.* **2018**, *1*, 3226−3235.

(39) Huang, L.; Jiang, Z.; Gong, W.; Shen, P. K. Facile Fabrication of Radial PtCo Nanodendrites for Enhanced Methanol Oxidation Electrocatalysis. *ACS Appl. Nano Mater.* **2018**, *1*, 5019−5026.

(40) Barroso, J.; Pierna, A. R.; Blanco, T. C.; Ruiz, N.; Sanchez, M. Anodic amorphous (NiNb)99(PtCu)1 alloys: Comparison between different particle sizes of catalysts for PEFMC. *Int. J. Hydrogen Energy* **2013**, *38*, 4079−4088.

(41) Barranco, J.; Pierna, A. R. Amorphous Ni59Nb40Pt(1 x)Yx (Y = Sn, Ru; x = 0%, 0.4%) modified carbon paste electrodes and their role in the electrochemical methanol deprotonation and CO oxidation process. *J. Non Cryst. Solids* **2007**, *353*, 851−854.

(42) Sistiaga, M.; Pierna, A. R. Application of amorphous materials for fuel cells. *J. Non Cryst. Solids* **2003**, *329*, 184−187.

(43) Ramos Sánchez, G.; Pierna, A. R.; Solorza Feria, O. Amorphous Ni59Nb40PtxM1 x (M = Ru,Sn) electrocatalysts for oxygen reduction reaction. *J. Non Cryst. Solids* **2008**, *354*, 5165−5168.

(44) Stanojevic, S.; Gallino, I.; Aboulfadl, H.; Sahin, M.; Mücklich, F.; Busch, R. Oxidation of glassy Ni Nb Sn alloys and its influence on the thermodynamics and kinetics of crystallization. *Acta Mater.* **2016**, *102*, 176−186.

(45) Sun, M.; Rauf, A.; Zhang, Y.; Sha, G.; Peng, G.; Yu, Z.; Guo, C.; Fang, Y.; Lan, S.; Feng, T.; Hahn, H.; Gleiter, H. Enhanced inter diffusion of immiscible elements Fe/Cu at the interface of FeZr/CuZr amorphous multilayers. *Mater. Res. Lett.* **2017**, *6*, 55−60.

(46) Mu, X.; Wang, D.; Feng, T.; Kübel, C. Radial distribution function imaging by STEM diffraction: Phase mapping and analysis of heterogeneous nanostructured glasses. *Ultramicroscopy* **2016**, *168*, 1−6.

(47) Yang, L.; Meng, X. f.; Guo, G. q. Structural origin of the pinpoint composition effect on the glass forming ability in the NiNb alloy system. *J. Mater. Res.* **2013**, *28*, 3170−3176.

(48) Evenson, Z.; Naleway, S. E.; Wei, S.; Gross, O.; Kruzic, J. J.; Gallino, I.; Possart, W.; Stommel, M.; Busch, R. β Relaxation and low temperature aging in a Au based bulk metallic glass: from elastic properties to atomic scale structure. *Phys. Rev. B: Condens. Matter Mater. Phys.* **2014**, *89*, 174204.

(49) Gallino, I.; Shah, M. B.; Busch, R. Enthalpy relaxation and its relation to the thermodynamics and crystallization of the Zr58.5Cu15.6Ni12.8Al10.3Nb2.8 bulk metallic glass forming alloy. *Acta Mater.* **2007**, *55*, 1367−1376.

(50) Enayati, M. H. Crystallization behavior of Ni Nb amorphous alloys. *Sci. Iran.* **2002**, *9*, 157−161.

(51) Fang, T.; Kennedy, S. J.; Quan, L.; Hicks, T. J. The structure and paramagnetism of nickel niobium (Ni3Nb). *J. Phys.: Condens. Matter* **1992**, *4*, 2405−2414.

(52) Cheshideh, H.; Nasirpouri, F. Cyclic voltammetry deposition of nickel nanoparticles on TiO2 nanotubes and their enhanced properties for electro oxidation of methanol. *J. Electroanal. Chem.* **2017**, *797*, 121−133.

(53) Tehrani, R. M. A.; Ab Ghani, S. The Nanocrystalline Nickel with Catalytic Properties on Methanol Oxidation in Alkaline Medium. *Fuel Cells* **2009**, *9*, 579−587.

(54) Qi, Z.; Geng, H.; Wang, X.; Zhao, C.; Ji, H.; Zhang, C.; Xu, J.; Zhang, Z. Novel nanocrystalline PdNi alloy catalyst for methanol and ethanol electro oxidation in alkaline media. *J. Power Sources* **2011**, *196*, 5823−5828.

(55) De, S.; Zhang, J.; Luque, R.; Yan, N. Ni based bimetallic heterogeneous catalysts for energy and environmental applications. *Energy Environ. Sci.* **2016**, *9*, 3314−3347.

(56) Chellali, M. R.; Nandam, S. H.; Li, S.; Fawey, M. H.; Moreno Pineda, E.; Velasco, L.; Boll, T.; Pastewka, L.; Kruk, R.; Gumbsch, P.; Hahn, H. Amorphous nickel nanophases inducing ferromagnetism in equiatomic Ni Ti alloy. *Acta Mater.* **2018**, *161*, 47−53.